OPEN ACCESS

High-frequency dynamics in the near-surface region studied by inelastic x-ray scattering: the case of liquid indium

To cite this article: Björn Wehinger *et al* 2011 *New J. Phys.* **13** 023021

New Journal of Physics
The open-access journal for physics

High-frequency dynamics in the near-surface region studied by inelastic x-ray scattering: the case of liquid indium

Björn Wehinger[1], **Michael Krisch and Harald Reichert**
European Synchrotron Radiation Facility, BP 220, F-38043 Grenoble Cedex, France
E-mail: wehinger@esrf.fr

New Journal of Physics **13** (2011) 023021 (20pp)
Received 22 October 2010
Published 9 February 2011
Online at http://www.njp.org/
doi:10.1088/1367-2630/13/2/023021

Abstract. Inelastic x-ray scattering in grazing angle geometry provides a novel tool for studying the surface and bulk lattice dynamics in a single experiment by varying the incidence angle around the critical angle of total reflection. At very small incidence angles (below the critical angle), it is possible to study the collective dynamics in a subsurface region of a few nanometres at interatomic length and time scales. An experimental study on liquid indium in the near-surface region is presented here and the results are analysed within a theoretical framework, based on classical hydrodynamics for the height–height fluctuations (capillary waves and non-propagating fluctuations) and generalized hydrodynamics for the bulk density fluctuations. The investigation reveals the presence of capillary waves in the inelastic x-ray spectra as an additional contribution at zero-energy transfer and a modification of the bulk density fluctuation contribution. A longer structural relaxation time and a larger longitudinal viscosity with respect to bulk indium are observed, similarly to related studies in confined liquids.

[1] Author to whom any correspondence should be addressed.

Contents

1. Introduction

Despite centuries of research, the study of the liquid state continues to provide us with new insights. In particular, surprising phenomena occur in confinement or at the surface of liquids. These include molecular ordering and orientation at the surface, layering at liquid metal surfaces on an atomic scale, surface freezing in liquid alkanes and alcohols, surface melting and pre-melting at the water surface, thermally excited height fluctuations (capillary waves) and visco-elastic surfaces waves [1]. Understanding the surface phenomena of liquids is of fundamental scientific interest, and there are also many technical applications, for example in nanotechnology, in conjunction with complex fluids such as polymers, surfactants, colour pigments, etc.

Examples of powerful tools for investigating the surface phenomena of liquids include visible light, neutron scatting and x-ray scattering [1]. With the advent of synchrotron x-ray sources, x-ray specular reflectivity [2] has been developed for the study of liquid surfaces on an atomic scale [3, 4], thus allowing for a unique insight into the arrangement of atoms through the observation of the electron distributions and their spatial fluctuations. The study of the microscopic dynamics at surfaces, however, is a largely unexplored research field. Established techniques comprise exclusively surface-sensitive techniques, such as electron-energy-loss spectroscopy and helium scattering [5, 6]. Compared to these, inelastic x-ray scattering (IXS) offers an attractive alternative. In fact, IXS directly probes the dynamical structure factor $S(\boldsymbol{q}, \omega)$, where $\boldsymbol{q}$ is the momentum transfer and ω the frequency, via the detection of the frequency shift of the scattered photons due to the creation and annihilation of vibrational quanta [7]. The accessible range in energy (1 meV to several hundreds of meV) and momentum transfer (1–100 nm^{-1}) corresponds to the picosecond time scale and inter-atomic distances, respectively. The depth-controlled investigation of near-surface atomic correlations can be achieved by scattering in grazing angle geometry [8]. Combining IXS with meV energy resolution and grazing angle geometry therefore allows the investigation of the microscopic dynamics at surfaces [9, 10]. This provides a unique possibility of selectively studying the bulk and surface dynamics in a single experiment by varying the incidence angle around the critical angle of total reflection.

The work presented here is focused on liquid indium, which exhibits clear surface phenomena of manageable complexity. At the liquid–vapour interface in liquid indium, the

potential energy of the electrons changes dramatically. In the bulk liquid phase, the electrons are delocalized, resulting in a screened Coulombic potential that acts on a short range, whereas in the vapour phase the electrons are localized, leading to a long-range van der Waals-type potential. The strong Coulombic interactions and the density variation at the liquid–vapour interface give rise to atomic layering [11]. This clear surface layering might also influence the microscopic dynamics and motivates the present study.

Following the first experiment on the high-frequency subsurface and bulk dynamics of liquid indium [10], we present here experimental data of superior quality because of improved sample preparation, and most importantly, at three different incidence angles, straddling the critical angle, thus spanning a probing depth from 4 to 180 nm. Moreover, an analysis that quantitatively takes into account contributions from the bulk and surface dynamics was employed.

This paper is organized as follows. The formalism that describes the near-surface dynamics by combining bulk and surface dynamics within a single frame is presented in section 2. Experimental details are given in section 3. The results are presented and discussed in section 4. Section 5 summarizes our findings and provides an outlook.

2. Theoretical background

2.1. Correlation functions and dynamical structure factor

The dynamics of the liquid state are the result of density fluctuations, which can be described via time correlation functions [12]. These functions take into account spatial and temporal variations and describe the thermal fluctuations in a fluid. The density–density correlation function is the thermodynamic average of the instantaneous density deviation from its average value at a given point in space and time. It reflects the thermodynamic, structural and transport properties of the fluid. The density–density correlation function in the mesoscopic regime—i.e. probing interatomic distances—can be determined by photon correlation spectroscopy [13], inelastic neutron scattering [14] or IXS [15], and results in a characteristic intensity distribution of the scattered signal as a function of momentum and energy transfer. Two types of fluctuations have to be taken into account: (i) density fluctuations in the isotropic bulk liquid and (ii) density fluctuations at the surface (height fluctuations) where the translational symmetry is broken. As there is no theoretical framework for the height–height fluctuations in the mesoscopic range, the correlation functions will be introduced in the hydrodynamic approach. The formalism for the bulk fluctuations is then presented within the framework of generalized hydrodynamics, which takes into account both the local arrangement and the interaction of the atoms [12].

2.1.1. Hydrodynamic limit. We follow the approach of Mora and Daillant [16] based on [17]–[19] using linear response theory and the fluctuation–dissipation theorem to relate the correlation in the fluctuations to the response of the system to an external perturbation.

The density–density and the height–height fluctuation spectra are, respectively,

$$\begin{aligned} C_{\rho\rho}(q,\omega) &= \int_{-\infty}^{\infty}\int_{-\infty}^{\infty} \frac{2k_{\mathrm{B}}T}{\omega} \operatorname{Im}\chi_{\rho\rho}(q,z,z',\omega)\,\mathrm{d}z'\,\mathrm{d}z \\ &= \frac{4\rho_0 k_{\mathrm{B}}T}{\omega^3} \frac{q^2\left(q_{\mathrm{i}}^2 q_{\mathrm{h}}^2 - q_{\mathrm{a}}^2 q_{\mathrm{h}}^2\right)}{\left(q^2-q_{\mathrm{h}}^2\right)\left(q^2-q_{\mathrm{a}}^2\right)} \end{aligned} \tag{1}$$

and

$$C_{zz}(q_\parallel,\omega) = \frac{2k_\mathrm{B}T}{\omega}\,\mathrm{Im}\,\chi_{zz}(q_\parallel,0,0,\omega)$$
$$= \frac{2k_\mathrm{B}T}{\omega}\mathrm{Re}\left[\left(\frac{q_h^2-q_i^2}{q_h^2-q_a^2}\frac{1}{q_a^z}+\frac{q_i^2-q_a^2}{q_h^2-q_a^2}\frac{1}{q_h^z}\right)\left(1-\frac{2q_\parallel^2}{q_t^2}\right)^2\rho_0\omega^2+q_\parallel^2\left(\frac{4\rho_0\omega^2q_t^z}{q_t^4}+\mathrm{i}\alpha\right)\right]^{-1}, \tag{2}$$

where $\chi_{\rho\rho}$ and χ_{zz} are the response tensors of the density–density and height–height fluctuations [16], $q_\parallel$ is the momentum transfer parallel to the surface, ρ_0 is the constant equilibrium density, k_B the Boltzmann constant, T the temperature, ω the frequency and α the surface tension. The transverse shear modes have wavevectors $q_\mathrm{t}^2 = \mathrm{i}\rho_0\omega/\eta$; the longitudinal modes $q_\mathrm{h}^2 = \mathrm{i}C_\mathrm{p}\omega/\kappa$, corresponding to heat diffusion, and $q_\mathrm{a}^2 = \omega^2/(v_\mathrm{a}^2 - \mathrm{i}\omega\gamma_\mathrm{a})$, with $\gamma_\mathrm{a} = (\zeta + \frac{4}{3}\eta)/\rho_0 + \kappa\left(C_\mathrm{p}/C_\mathrm{V} - 1\right)/C_\mathrm{p}$, denote the damped propagating acoustic waves; $q_\mathrm{i}^2 = \omega^2/(v_\mathrm{i}^2 - \mathrm{i}\omega\gamma_\mathrm{i})$ with $v_\mathrm{i}^2 = C_\mathrm{V}v_\mathrm{a}^2/C_\mathrm{p} = 1/(\rho_0\kappa_\mathrm{T})$ and $\gamma_\mathrm{i} = (\zeta + \frac{4}{3}\eta)/\rho_0$ is the isothermal acoustic wavevector. η and ζ are the shear and bulk viscosities, respectively, $C_\mathrm{p}$and C_V the specific heat at constant pressure and constant volume, respectively; κ the thermal conductivity, v_a the adiabatic sound velocity and κ_T the isothermal compressibility. The z-components of the wavevectors (perpendicular to the surface) are given through the relation $q_{\mathrm{a,h,t}}^z = \sqrt{q_{\mathrm{a,h,t}}^2 - q_\parallel^2}$.

The shape of the height–height fluctuation spectrum can be approximated by a Lorentzian in the low-q region for small viscosities [20], more specifically, if $\eta q^2/\rho_0 \ll \omega_\mathrm{r}$, where ω_r is the ripple (capillary wave) frequency. This approach is justified in the case of IXS ($1\,\mathrm{nm}^{-1} < q < 20\,\mathrm{nm}^{-1}$) on the surface of liquid metals. The height–height fluctuation spectrum reduces then to

$$C_{zz}(q_\parallel,\omega) \approx \frac{k_\mathrm{B}Tq_\parallel}{\rho_0\omega_\mathrm{r}^2}\frac{\rho_0\omega_\mathrm{r}^2}{2\pi\,\eta q_\parallel^2\left(\omega^2+\left(\frac{\rho_0\omega_\mathrm{r}^2}{2\eta q_\parallel^2}\right)^2\right)}, \tag{3}$$

a Lorentzian with a width of $\Delta\omega = \rho_0\omega_\mathrm{r}^2/(\eta q_\parallel^2) = \alpha q_\parallel/\eta$ centred at zero frequency.

The dynamical structure factor in the hydrodynamical limit can be calculated using the fluctuation-dissipation theorem leading to

$$S(q,\omega) = A\frac{2k_\mathrm{B}T}{\omega}\,\mathrm{Im}\,\chi_{zz}(q_\parallel,0,0,\omega) + \frac{A}{\rho_0^2}\int_{-\infty}^{u_z(\boldsymbol{r}_\parallel,\omega)} \mathrm{e}^{z/\Lambda}\,\mathrm{d}z$$
$$\times\int_{-\infty}^{u_z(\boldsymbol{r}_\parallel,\omega)}\int_{-\infty}^{u_{z'}(\boldsymbol{r}_\parallel,\omega)}\frac{2k_\mathrm{B}T}{\omega}\,\mathrm{Im}\,\chi_{\rho\rho}(q,z,z',\omega)\,\mathrm{d}z'\,\mathrm{d}z, \tag{4}$$

where A is the illuminated area, Λ the scattering depth and $u_z(\boldsymbol{r}_\parallel,\omega)$ the time Fourier transform of the vertical liquid displacement at $\boldsymbol{r}_\parallel$ and time t. The shape of $S(q,\omega)$ does not change significantly for different $u_z(\boldsymbol{r}_\parallel,\omega)$ and a scattering depth Λ of the order of several nanometres. Furthermore, the energy integrated contribution of the coupling between density fluctuations and capillary waves can be estimated to be $\Lambda^{-1}\sqrt{k_\mathrm{B}T/\alpha}$ [16]. This is of the order of a few per cent for the smallest scattering depth investigated in the present study (4 nm). We therefore neglect this coupling, which is equivalent to setting the upper integration limits in equation (4) to zero. The dynamical structure factor is then given by

$$S(q,w) = AC_{zz}(q_\parallel,\omega) + \frac{A\Lambda}{2\rho_0^2}C_{\rho\rho}(q,\omega) = S(q_\parallel,w)_{zz} + S(q,w)_{\rho\rho}. \tag{5}$$

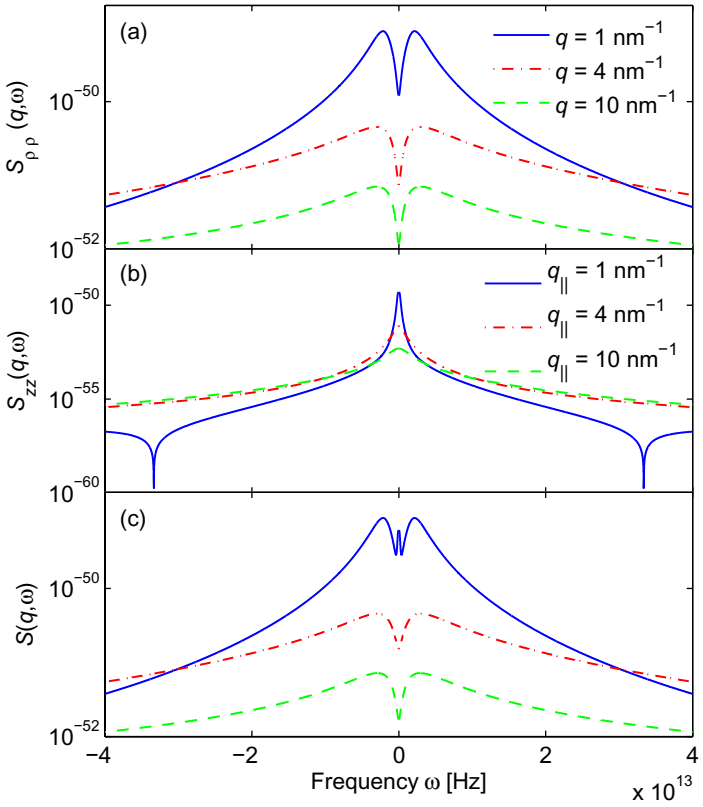

Figure 1. (a) Bulk and (b) surface contributions of the dynamical structure factor for three different momentum transfers and a scattering depth of 4 nm. (c) Total dynamical structure factor $S_{\rho\rho}(q, \omega) + S_{zz}(q_{\|}, \omega)$.

Figure 1 shows the density–density and height–height fluctuation contributions to the dynamical structure factor for liquid indium at 170 °C, using thermodynamic parameters taken from the literature [21]–[26]. In figure 1(a), the apparent peaks in the density–density contribution are associated with the propagating acoustic waves. The transverse waves are completely suppressed in the momentum transfer range of interest. The acoustic peak becomes broader for increasing momentum transfer. The height–height contribution in figure 1(b) shows the capillary wave contribution to the dynamical structure factor in the form of a Lorentzian around zero energy transfer. The capillary wave excitation is overdamped for momentum transfers $q > 1\,\mathrm{nm}^{-1}$; the remaining effect is a shift in the surface acoustic peak towards higher frequency. This cannot be seen in the plot because the surface acoustic excitation is very broad with low intensity. An additional dip appears at higher frequencies due to the resonance of the heat diffusion and the acoustic wave. The overall correlation function near the surface is a combination of both the density–density and the height–height correlation function. The total dynamical structure factor is shown in figure 1(c). The bulk acoustic peak is more intense and sharper than the surface acoustic one. It is therefore extremely difficult to observe the shifted surface acoustic excitation as an additional peak in a momentum transfer range of $1\,\mathrm{nm}^{-1} < q < 10\,\mathrm{nm}^{-1}$. The situation is different for the central frequency peak (elastic line): the surface contribution appears as an additional Lorentzian to the elastic line with respect to the bulk spectra.

2.1.2. Generalized hydrodynamics. In the mesoscopic range both the local arrangement and the interaction of the atoms influence the dynamics of a bulk liquid. Whereas to date a formally exact description in this regime does not exist, the memory function formalism [27, 28] describes quite well the observed phenomenology.

The dynamical structure factor in the memory function approach reads

$$\frac{S(q,\omega)}{S(q)} = \frac{1}{\pi}\frac{(v_T(q)q)^2 m'_{\mathrm{L}}(q,\omega)}{[\omega^2 - (v_{\mathrm{T}}(q)q)^2 - \omega m''_{\mathrm{L}}(q,\omega)]^2 + \omega^2[m'_{\mathrm{L}}(q,\omega)]^2}, \tag{6}$$

where v_{T} is the isothermal sound velocity, $m'_{\mathrm{L}}(q,\omega)$ and $m''_{\mathrm{L}}(q\omega)$ are the real and imaginary parts of the memory function in Fourier space and

$$S(q) = \int_{-\infty}^{\infty} S(q,\omega)\,\mathrm{d}\omega. \tag{7}$$

In the case of liquid metals, the memory function features three terms describing different decay mechanisms,

$$m_{\mathrm{L}}(q,t) = (\gamma(q)-1)(v_{\mathrm{T}}(q)q)^2\delta(t) + \Delta^2_\alpha(q)\mathrm{e}^{-t/\tau_\alpha(q)} + \Delta^2_\mu(q)\mathrm{e}^{-t/\tau_\mu(q)}, \tag{8}$$

where $\Delta_{\alpha,\mu}$ are the strengths of the structural and microscopic relaxation, respectively, and $\tau_{\alpha,\mu}$ the corresponding relaxation times. The first relaxation term in the memory function corresponds to a dissipation process via thermal diffusion and is therefore called thermal relaxation. The local density change of the liquid leads to a small temperature shift that is equalized by a heat transfer through the surface surrounding the compressed volume. In liquid metals, this mechanism becomes very efficient in the momentum transfer range observed in an IXS process [29]. The thermal diffusivity D_{T} of liquid indium is very high, which allows approximation of this decay by a δ-function [30]. The structural relaxation is caused by the cooperative rearrangement of the disordered structure, which influences the dynamics on a time scale of the order of picoseconds [31]. Interatomic interactions, such as collisions and attractive potentials, determine this process. The origin of the energy transfer can be explained by using mode coupling theory [32]. A comparison with the hydrodynamic limit leads to the relation $v_\infty^2 - v_{\mathrm{a}}^2 = \Delta_\alpha^2/q^2$, where v_∞ is the infinite frequency sound velocity in the totally unrelaxed regime and v_{a} the adiabatic sound velocity in the fully relaxed regime. The microscopic relaxation is associated with internal degrees of freedom and corresponds to vibrations in monoatomic liquids. The respective time scale is expected to be an order of magnitude smaller than for the structural relaxation. For probing the system on time scales that are much shorter than the relaxation time, the plane waves that excite the system are not eigenstates of the disordered system. This induces an energy transfer between the exciting plane waves and normal modes of the disordered structure.

The real and imaginary parts of the memory function in Fourier space are given by

$$m'_{\mathrm{L}}(q,\omega) = (\gamma(q)-1)(v_{\mathrm{T}}(q)q)^2 + \Delta^2_\alpha(q)\frac{\tau_\alpha(q)}{1+(\omega\tau_\alpha(q))^2} + \Delta^2_\mu(q)\frac{\tau_\mu(q)}{1+(\omega\tau_\mu(q))^2} \tag{9}$$

and

$$\omega m''_{\mathrm{L}}(q,\omega) = (\gamma(q)-1)(v_{\mathrm{T}}(q)q)^2 + \Delta^2_\alpha(q)\frac{(\omega\tau_\alpha(q))^2}{1+(\omega\tau_\alpha(q))^2} + \Delta^2_\mu(q)\frac{(\omega\tau_\mu(q))^2}{1+(\omega\tau_\mu(q))^2}. \tag{10}$$

A relation for the longitudinal viscosity η_L can be derived by comparing the time integrals of the viscous part of the hydrodynamic memory function with the proposed memory function [28],

$$\eta_L(q) = \eta_\alpha + \eta_\mu = \frac{\rho_0}{q^2}[\Delta_\alpha^2(q)\tau_\alpha(q) + \Delta_\mu^2(q)\tau_\mu(q)]. \tag{11}$$

2.2. *Inelastic x-ray scattering (IXS) in grazing angle geometry*

The double differential cross-section for IXS, which determines the scattered intensity $I(\alpha_i, \alpha_f)$, is given by

$$\frac{d^2\sigma}{d\Omega\, d\omega} = r_e^2\rho_e^2|T_{i,0,1}|^2|T_{f,0,1}|^2(\hat{\boldsymbol{e}}_i \cdot \hat{\boldsymbol{e}}_f)^2 S(q, \omega), \tag{12}$$

where $\alpha_{i,f}$ are the incidence and exit angles, r_e is the classical electron radius, ρ_e is the average electron density, and $\hat{\boldsymbol{e}}_{i,f}$ are the polarization vectors of the incoming and outcoming beams, respectively. $T_{i,0,1}$ and $T_{f,0,1}$ are the roughness-corrected transmission functions [33] between the upper (0) and the lower (1) media, which can be found by assuming that the capillary waves create a rough surface with a Gaussian distribution for the z-coordinates of the surface,

$$T_{i,0,1} = \frac{2k_{iz,0}}{k_{iz,0} + k_{iz,1}} e^{1/2(k_{iz,1} - k_{iz,0})^2\varrho^2}, \tag{13}$$

where ϱ denotes the roughness parameter. For $T_{f,0,1}$, one has to change the index i to f.

In grazing angle x-ray scattering, the scattering depth Λ determines the region from which the observed scattering originates. As a consequence of reciprocity, both the incident and scattered x-rays enter symmetrically this quantity [8],

$$\Lambda(\alpha_i, \alpha_f) \equiv \frac{1}{|\mathrm{Im}\, q_{z,1}|} = l_{iz,1}(\alpha_i) + l_{fz,1}(\alpha_i, \alpha_f), \tag{14}$$

where $q_{z,1}$ is the momentum transfer in the lower medium perpendicular to the surface, $l_{iz,fz} = |\mathrm{Im}(k_{iz,fz})|^{-1}$ is the penetration depth of the evanescent incidence and exit wave in the medium perpendicular to the surface, and $\boldsymbol{k}$ denotes the wavevector. In a typical experiment, the incoming wavevector is defined very precisely, but the accuracy of the exit wavevector is limited by the aperture of the detector (in our case the aperture in front of the crystal analyser). The effective scattering depth is therefore the integral over the exit angle range spanned by the detector, weighted by the corresponding intensity contribution,

$$\Lambda_{\mathrm{eff}}(\alpha_i) = \frac{1}{I_{\mathrm{tot}}(\alpha_i)} \int_{\delta\alpha_f} \left(l_{iz,1}(\alpha_i) + l_{fz,1}(\alpha_i, \alpha_f)\right) I(\alpha_i, \alpha_f)\, d\alpha_f. \tag{15}$$

$\delta\alpha_f$ is the angular detector opening, $I(\alpha_i, \alpha_f) \sim |T_{i,0,1}|^2|T_{f,0,1}|^2 S(q, \omega)$ the α_f-resolved intensity and $I_{\mathrm{tot}}(\alpha_i) = \int I(\alpha_i, \alpha_f)\, d\alpha_f$ the total integrated intensity. The only term in $S(q, \omega)$ that shows a $\alpha_{i,f}$-dependence is the scattering depth Λ (see equations (5) and (14)). To calculate the effective scattering depth, one can therefore use the energy integrated differential cross-section, which can be formally derived for height fluctuations and density fluctuations [16],

$$\left(\frac{d\sigma}{d\Omega}\right)_{zz} = A r_e^2\rho_e^2|T_{i,0,1}|^2|T_{f,0,1}|^2(\hat{\boldsymbol{e}}_i \cdot \hat{\boldsymbol{e}}_f)^2 \frac{k_B T}{\alpha q_\parallel^2} \tag{16}$$

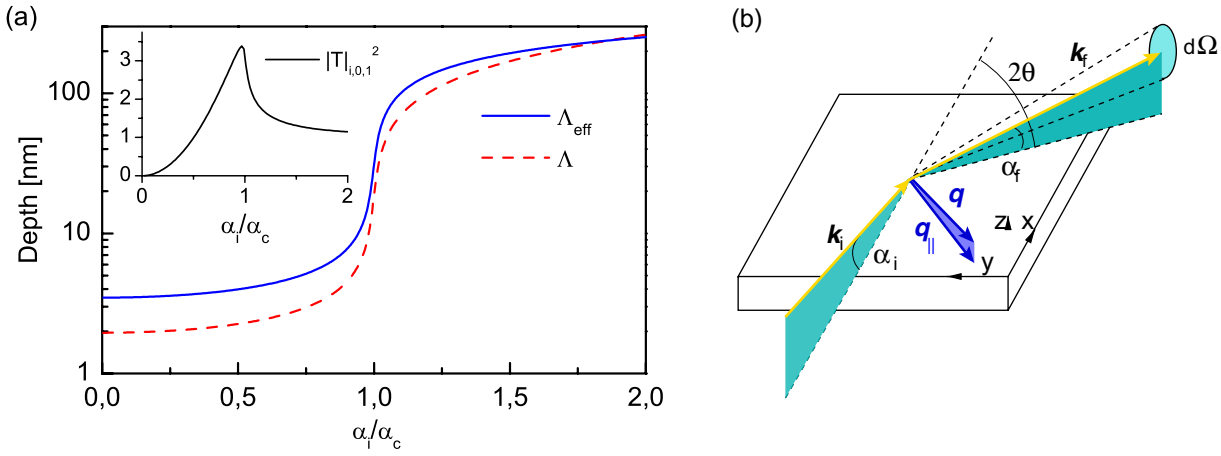

Figure 2. (a) The effective scattering depth for liquid indium at 170 °C for a detector opening of $\alpha_f = 0$–0.50° (solid blue line) and the scattering depth for an ideal point detector with $\alpha_f = \alpha_i$ (dashed red line). $\alpha_c = 0.163^\circ$ for an x-ray energy of 17.794 keV. The inset shows the transmission function of the incoming beam. (b) Scattering geometry in the grazing angle condition.

and

$$\left(\frac{d\sigma}{d\Omega}\right)_{\rho\rho} = A r_e^2 \rho_e^2 |T_{i,0,1}|^2 |T_{f,0,1}|^2 (\hat{\boldsymbol{e}}_i \cdot \hat{\boldsymbol{e}}_f)^2 k_B T \kappa_T \Lambda. \tag{17}$$

The total differential cross-section due to surface and bulk fluctuations is the sum of both the contributions. The α_f-resolved and energy integrated intensity is thus given by

$$I(\alpha_i, \alpha_f) \sim |T_{i,0,1}|^2 |T_{f,0,1}|^2 \left(\frac{1}{\alpha q_\parallel^2} + \kappa_T \Lambda(\alpha_i, \alpha_f)\right). \tag{18}$$

The same consideration must be applied to the vertical momentum transfer. The effective momentum transfer perpendicular to the surface is therefore

$$q_{z,\mathrm{eff}} = \frac{1}{I_{\mathrm{tot}}} \int_{\delta\alpha_f} (k_{fz}(\alpha_i, \alpha_f) - k_{iz}(\alpha_i)) I(\alpha_i, \alpha_f)\, d\alpha_f. \tag{19}$$

The effective scattering depth is typically of the order of a few nanometres, which is just of the same order of magnitude as typical correlation lengths of surface-induced phenomena. Another advantage of the grazing angle geometry is the enhancement of the evanescent wave field for incidence angles close to the critical angle providing sufficient intensity to perform inelastic scattering experiments. Figure 2(a) shows the scattering depth for liquid indium at 170 °C and a momentum transfer $q_\parallel = 4\,\mathrm{nm}^{-1}$ together with the roughness-corrected transmission function ($\varrho = 3$ Å) for the incoming x-rays. Note the difference between the real experimental conditions (Λ_{eff}) and the theoretical value (Λ) for an ideal point detector (no spread in α_f), and the strong variation around α_c. The scattering geometry is shown in figure 2(b). It is worth noting that the momentum transfer lies predominantly in the surface plane owing to the fact that both scattering angles (incident and exit) must be grazing. By varying the incident angle α_i within a few mrad around the critical angle of total reflection α_c, the surface and bulk dynamics are selectively probed in a single experiment.

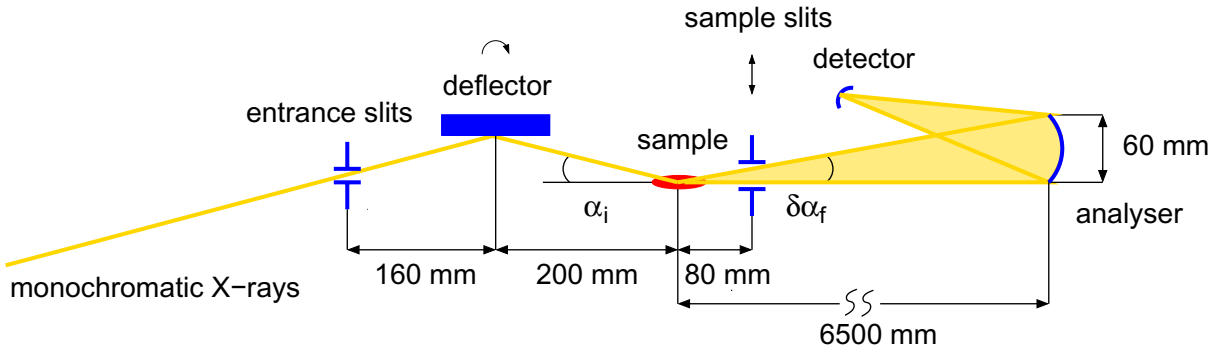

Figure 3. Schematic representation of the IXS setup in surface-sensitive geometry.

An interesting quantity is the ratio between the surface and bulk contributions,

$$\frac{I_{\text{surf}}}{I_{\text{bulk}}} = \frac{\left(\frac{\mathrm{d}\sigma}{\mathrm{d}\Omega}\right)_{zz}}{\left(\frac{\mathrm{d}\sigma}{\mathrm{d}\Omega}\right)_{\rho\rho}} = \frac{1}{\alpha\kappa_{\mathrm{T}}\Lambda_{\text{eff}}q_{\parallel}^2}. \tag{20}$$

For an effective scattering depth of 4 nm, one obtains for liquid indium (at 170 °C) equal contributions for $q_{\parallel} = 3.9\,\text{nm}^{-1}$.

3. Experimental details

The IXS experiment in grazing angle geometry was carried out on beamline ID28 at the European Synchrotron Radiation Facility (Grenoble, France). The IXS spectrometer was operated in the Si(9 9 9) configuration with $E = 17.794\,\text{keV}$, $\Delta E = 3.0\,\text{meV}$ and a flux of $2.7 \times 10^{10}\text{photons}\,\text{s}^{-1}$. The monochromatic beam was focused in the horizontal and vertical planes by a platinum-coated toroidal mirror, located 25 m from the sample. This scheme provides a focus at the sample position of $270 \times 60\,\mu\text{m}^2$ at full-width at half-maximum. The beam size was further reduced by slits to limit the footprint on the sample to 25 mm. The deflection angle of a platinum-coated mirror, inserted 200 mm in front of the sample position, defined the incidence angle on the sample. α_i could be changed by a combined variation of the toroidal and deflector mirror angles, together with a height correction of the entrance slit. This allowed us to keep the sample height and position fixed. Figure 3 shows schematically the inelastic x-ray spectrometer in surface-sensitive geometry. Further details can be found in [34, 35].

Liquid indium is the ideal material for studying the high-frequency dynamics in surface-sensitive scattering geometry because of its interesting oxidation behaviour [11], its low melting point (156 °C) and the extremely low vapour pressure ($\ll 10^{-13}$ mbar at 170 °C [36]). The oxidation of liquid indium is remarkable: under low oxygen dose, it forms macroscopic oxide islands observable by the eye, whereas the rest of the surface remains oxide-free. The very low vapour pressure of liquid indium implies that the free surface can be accessed instead of a liquid–vapour interface. Furthermore, a sufficiently strong signal is obtained even when probing only 4 nm, as the IXS cross-section is proportional to Z^2 at low q, where Z is the atomic number.

A very clean surface can be realized by using a carefully prepared and specially designed ultrahigh vacuum (UHV) chamber with beryllium entrance and exit windows for the x-rays.

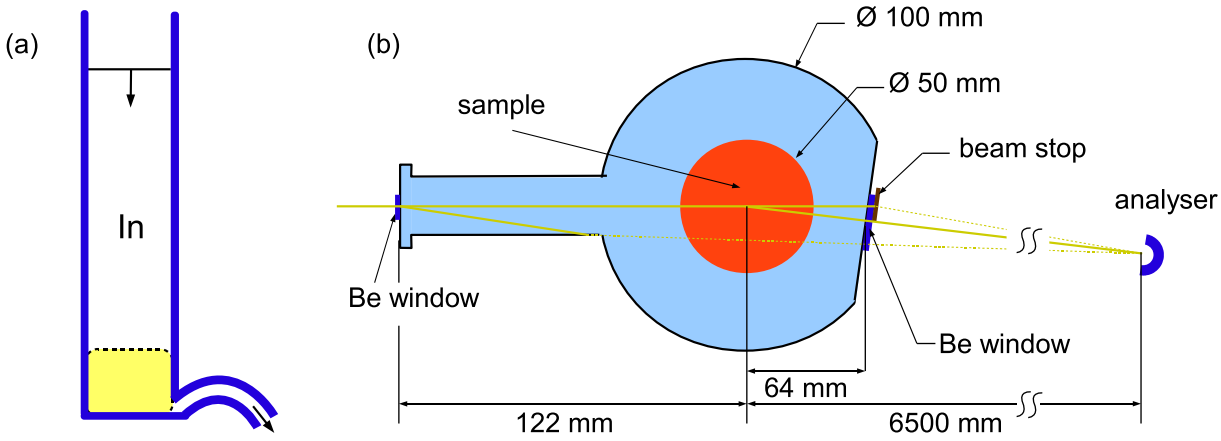

Figure 4. (a) Sketch of the glass vessel. The arrows indicate the flow of the liquid indium (In) during the melting process. The levels before and after the pouring are displayed by the continuous and dashed line, respectively. Due to the high surface tension and the missing air pressure under vacuum, the level of the remaining indium is higher than the outlet. The yellow area represents the remaining indium. The dimensions of the glass vessel are 25×70 mm. (b) Transverse section through the sample chamber (top view) and sketch of the suppression of parasitic scattering. The beryllium entrance window has been positioned as far as possible from the sample to avoid parasitic scattering from the beryllium. The beam stop that is placed directly after the exit window absorbs both the beryllium scattering and the direct beam.

Highly pure indium (50 g with a purity of 99.99999% from MCP, Alperton Middlesex, UK) was used. Prior to inserting it into the UHV chamber, it was necessary to remove organic contaminants and the 80–100 Å self-passivating film of oxide. This was accomplished by degreasing the solid indium with acetone in a 10 min ultrasonic bath to remove the organic contaminants. The surface was then mildly etched in a 10% hydrochloric acid solution (by volume) for 5 min until the surface appeared shiny. Following this, the acid was thoroughly rinsed twice with deionized water and acetone, respectively. The sample was then dried by nitrogen gas and inserted into the glass vessel. Indium oxide has the particular property of adhering on the glass vessel. The pure indium, by contrast, does not stick to the glass and flows out. A bent outlet ensured that only clean indium flowed into the sample trough while the top oxide-covered indium portion remained in the glass vessel. Figure 4(a) illustrates the principle of the system. The glass vessel was resistively heated and temperature controlled by a NiCr–Ni thermocouple.

After closing the specially designed UHV chamber (see figure 4(b)), the system was baked for 3 days at 140 °C. The base pressure before the experiment was 2×10^{-9} mbar. With a diameter of 50 mm, the sample trough (highly pure molybdenum) was large enough to guarantee a sufficiently flat liquid surface in the illuminated area of 270 μm $\times$ 25 mm. The sample trough was cleaned after the bake-out period by 20 min sputtering at 1.47 keV beam energy and an argon pressure of 4×10^{-6} mbar. This provided a sputter current of 80 μA, sufficiently high to remove all contaminants from the trough prior to filling the trough with liquid indium.

For the IXS measurements, the UHV chamber was mounted on a vibration-isolation stage, which was fixed on the goniometer of the inelastic scattering setup. The indium was melted by heating the glass vessel after mounting the chamber. The sample trough was resistively heated and temperature monitored by a NiCr–Ni thermocouple. The heating of the sample trough during the measurement to 170 °C caused more out-gassing, which resulted in a pressure increase to 1×10^{-8} mbar. For the estimated oxygen partial pressure of $\approx 10^{-11}$ mbar, the time to grow an oxide monolayer was calculated to be approximately 8 days [36]. Indeed, after the 1 week experiment, visual inspection revealed that one small oxide island was formed, located outside of the illuminated area. The possible influence of an oxide island drifting into the beam path can be estimated as follows. The scattering cross-section of indium oxide is similar to the cross-section of pure indium, the intensity contribution is thus of the same order for equal scattering volume. The illuminated area is 270 μm $\times$ 25 mm with a minimal scattering depth of 4 nm. Due to the large footprint, an oxide island with a diameter of 1 mm and a thickness of 2 nm would contribute approximately 2% to the total signal.

IXS spectra were recorded at three different incidence angles ($\alpha_i = 0.5\alpha_c = 0.08^\circ$, $\alpha_i = 0.9\alpha_c = 0.15^\circ$ and $\alpha_i = 1.4\alpha_c = 0.23^\circ$), corresponding to an effective scattering depth of 4, 8 and 180 nm, respectively (see equation (15)). For each angle of incidence, spectra at eight different scattering angles were collected simultaneously.

The efficient suppression of parasitic scattering was probed by an empty cell measurement at momentum transfers used in the experiment and for various positions of the beamstop. In all cases, the contribution was negligible compared to the signal from the sample.

4. Results and discussion

Representative IXS spectra for several momentum transfers and the three angles of incidence are shown in figure 5. The experimental data and their respective error bars are plotted together with the corresponding best-fit result. The spectra show a clear dependence of the capillary wave contribution as a function of momentum transfer and scattering depth. Broadening of the excitation width with increasing momentum transfer and a slight broadening of the excitations with increasing scattering depth are noticeable. A third aspect is a slight narrowing of the elastic peak in the density fluctuation contribution with increasing scattering depth.

The intensity of the observed spectra is related to the dynamic structure factor via

$$I(q,\omega) = A(q)[n(\omega,T)S(q,\omega) \otimes R(\omega)] + B(q,\omega), \tag{21}$$

where $\otimes$ denotes the convolution operator and $n(\omega, T)$ is the detailed balance factor

$$n(\omega,T) = \frac{\hbar\omega/k_B T}{1 - e^{-\hbar\omega/k_B T}}. \tag{22}$$

$R(\omega)$ is the experimental resolution function and $A(q)$ is a factor taking into account the scattering geometry, the experimental setup and the atomic form factor. $B(q,\omega)$ takes into account the background of the electronics and the environment. The analytical form of $S(q,\omega)$ is given by equation (6) using (9) and (10). The contribution of the capillary waves to the $\alpha_i = 0.5\alpha_c$ and $\alpha_i = 0.9\alpha_c$ data sets is taken into account by including a Lorentzian function in the expression for the dynamical structure factor,

$$I(q,\omega) = A(q)[n(\omega,T)(S(q,\omega) + L(q,\omega)) \otimes R(\omega)] + B(q,\omega). \tag{23}$$

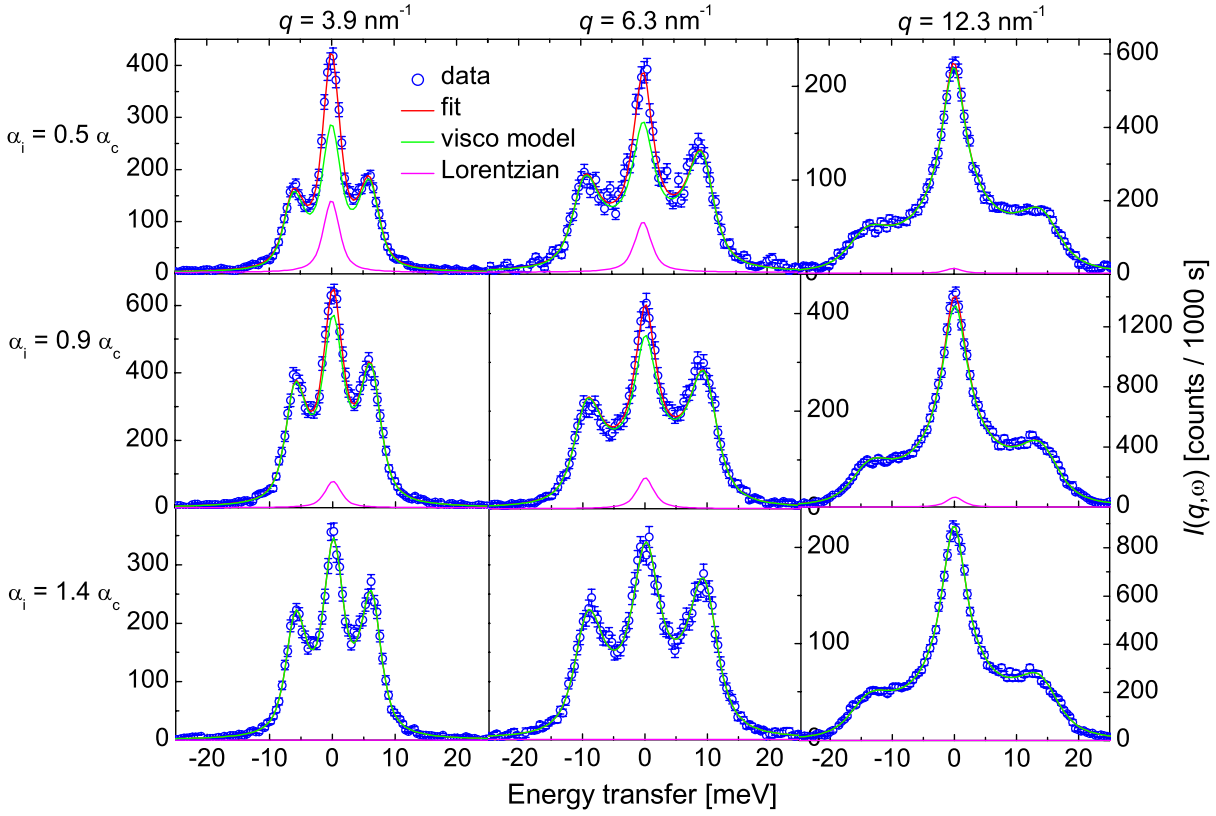

Figure 5. IXS spectra for momentum transfers of $3.9\,\mathrm{nm}^{-1}$ (left column), $6.3\,\mathrm{nm}^{-1}$ (middle column) and $12.3\,\mathrm{nm}^{-1}$ (right column). The experimental data (blue circles) are shown together with their best fit result (red lines) for the three different incidence angles. The dynamical structure factor convoluted with the experimental resolution function (fit) is the sum of the contributions of density fluctuations (green) and capillary waves (magenta).

The analytical form of $L(q,\omega)$ is given by equation (3). This approximation was obtained in the hydrodynamical limit. Since this limit is not strictly valid in the present study, the fits were performed using a Lorentzian function with free fitting parameters instead of including the analytical formula in the expression for the dynamical structure factor.

The fitting procedure (MINUIT software [37]) is based on a standard minimization of χ^2. The errors are calculated via the Hessian and covariance matrices.

In order to reduce the correlation between the fitting parameters, the temperature T was fixed at the measured value and the specific heat ratio was set to $\gamma = 1$, a value very close to the actual value of 1.08. Within this approximation, the term for the thermal relaxation vanishes in equation (8). The free fitting parameters are the overall intensity factor $A(q)$, a background $B(q)$ independent of the energy transfer, the isothermal and infinite frequency dispersion $\Omega_\mathrm{T}(q) = v_\mathrm{T} q$ and $\Omega_\infty(q) = v_\infty q$ that determine the strength of the structural relaxation $\Delta_\alpha^2(q) = \Omega_\infty^2 - \gamma\Omega_\mathrm{T}^2$, the structural relaxation time τ_α, the strength of the microscopic relaxation Δ_m^2 and the microscopic relaxation time τ_m. The influence of the surface contribution is negligible for an effective scattering depth of 180 nm ($\alpha_\mathrm{i} = 1.4\alpha_\mathrm{c}$). This is proven by performing fits without

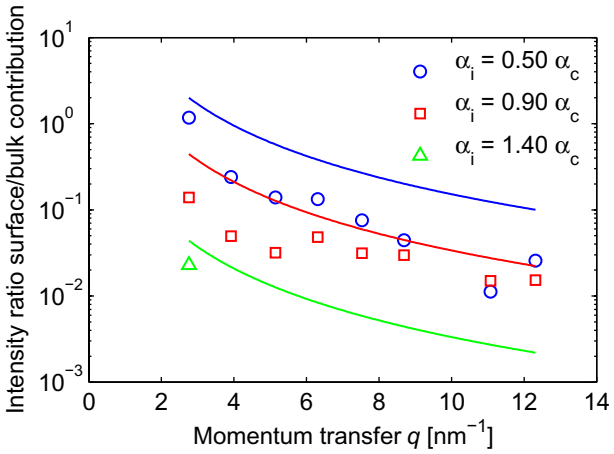

Figure 6. Experimental (open symbols) and theoretical intensity ratios in the hydrodynamic limit (solid lines) between the surface and bulk contributions for the measured incidence angles. The ratio for $\alpha_i = 1.4\alpha_c$ has been kept to zero for all momentum transfer values except for $q = 2.8\,\mathrm{nm}^{-1}$. A precise error estimation could not be performed due to the strong correlation of the fitting parameters and the fact that the fit was performed in two steps (see text for further details).

an additional Lorentzian. The obtained fitting parameters are in agreement with the results of the previous measurement in transmission geometry [10].

For modelling the surface-sensitive spectra at $\alpha_i = 0.5\alpha_c$ and $\alpha_i = 0.9\alpha_c$, the obtained fit parameters from the bulk spectra were first kept fixed (except the intensity factor and the background), and a Lorentzian function was fitted to the elastic line. In the second step, the obtained Lorentzian was fixed and the parameters of the visco-elastic model were left free. This procedure estimates the capillary wave contribution most accurately, and reduces the parameter correlation between the contributions of height and density fluctuations.

Figure 6 shows the calculated (lines) and experimental (symbols) intensity ratios of the surface contribution to the bulk contribution. The bulk density fluctuations dominate the scattering contribution for $\alpha_i = 1.4\alpha_c$ even for low momentum transfers. The IXS spectra in surface-sensitive geometry ($\alpha_i = 0.5\alpha_c$ and $\alpha_i = 0.9\alpha_c$) are influenced by height fluctuations in the low momentum region. The depth and momentum transfer dependence of the intensity ratio is qualitatively well reproduced by equation (20) (see solid lines in figure 6). The experimental points lie, however, systematically below the calculated curve. This can be partly ascribed to the fact that the hydrodynamic model, in contrast to the visco-elastic model within the generalized hydrodynamic framework, does not show any spectral intensity around zero energy transfer (see figure 1). The discrepancy is largest for $\alpha_i = 0.9\alpha_c$. A small error in α_i around α_c leads in fact to a large change in Λ_{eff}, which we estimate to be $^{+10}_{-1.8}$ nm. A common scaling factor of approximately two for all three incidence angles is obtained by setting $\Lambda_{\mathrm{eff}} = 18\,\mathrm{nm}$ for $\alpha_i = 0.9\alpha_c$ and taking the nominal effective scattering depth from equation (15) for $\alpha_i = 0.5\alpha_c$ ($\Lambda_{\mathrm{eff}} = 4\,\mathrm{nm}$) and $\alpha_i = 1.4\alpha_c$ ($\Lambda_{\mathrm{eff}} = 180\,\mathrm{nm}$). We therefore use $\Lambda_{\mathrm{eff}} = 18\,\mathrm{nm}$ for $\alpha_i = 0.9\alpha_c$ in the following.

The dispersion relations and sound velocities as obtained from the fit parameters are reported in figure 7(a). The apparent (or longitudinal) dispersion can be calculated from

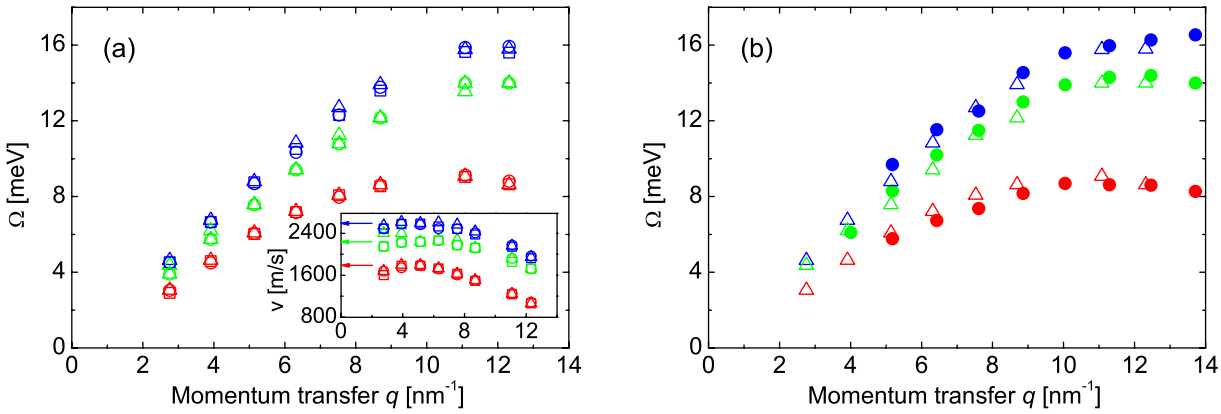

Figure 7. (a) Isothermal (red), infinite frequency (blue) and apparent (green) dispersion and sound velocities (insert) for different scattering depths: $\Lambda_{\text{eff}} = 4\,\text{nm}$ (circles), $\Lambda_{\text{eff}} = 18\,\text{nm}$ (squares) and $\Lambda_{\text{eff}} = 180\,\text{nm}$ (triangles). The zero momentum transfer limits are indicated by the arrows. The values at the smallest momentum transfer ($q = 2.8\,\text{nm}^{-1}$) are too low. Here, the excitation energy is comparable to the energy resolution, thus rendering the fit very difficult and unreliable. The errors are in the order of the symbol size and are not reported for clarity. (b) Comparison of the isothermal (red), infinite frequency (blue) and apparent (green) dispersion relations for $\Lambda_{\text{eff}} = 180\,\text{nm}$ (open triangles) with the bulk values derived from [10] (full circles).

the dynamical structure factor. It is the momentum transfer dependence of the excitation energy and corresponds to the maxima of the longitudinal current correlation function $J_l(q, \omega) = \omega^2 S(q, \omega)/q^2$. The dispersion relations are in good agreement with the previous bulk measurement in transmission geometry [10] (see figure 7(b)). The longitudinal (or apparent) dispersion is systematically higher than the isothermal one. This is a common behaviour in the visco-elastic regime and observed in many other liquids [29, 38]. The form of the sound dispersion curves can be understood in analogy to crystalline systems. The first sharp diffraction peak of the liquid can be interpreted similar to the Bragg reflection in a crystal. The sound dispersion should then follow a sinusoidal shape up to the 'Brillouin zone edge' that is located at half the distance from the first sharp diffraction peak in reciprocal space. The fit parameters follow this model-independent behaviour up to a momentum transfer of $11.5\,\text{nm}^{-1}$, which is half the distance to the first maximum of the structure factor at $23\,\text{nm}^{-1}$ for liquid indium. In contrast to the first surface-sensitive IXS experiment on liquid indium [10], we could not confirm changes of the dispersion relation in the near-surface region. The obtained zero-momentum transfer limits for the isothermal, infinite and apparent sound velocities are comparable to previous measurements [39].

The fit results for the structural and microscopic relaxation times are presented in figures 8(a) and (b). The error bars are quite large, but a trend to longer relaxation times at the surface in comparison to the bulk is indeed apparent. The relaxation times of this work are compared to the values derived from [10] in figures 8(c) and (d). The results agree within the error bars. Since the bulk and surface measurements were carried out in a single experiment by only varying the angle of incidence, it can be excluded that the obtained changes are due to differences in the experimental setup. The increase in the structural relaxation time at

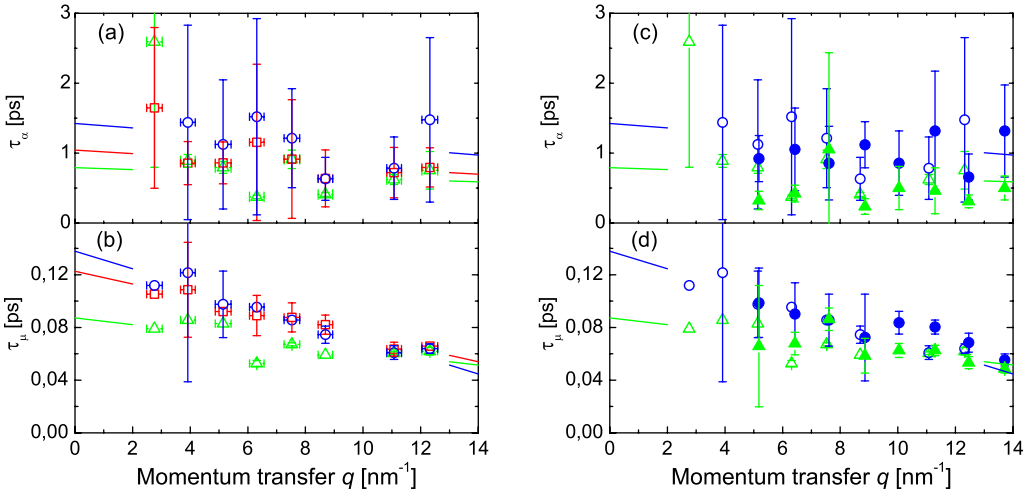

Figure 8. Structural (a) and microscopic (b) relaxation times for different scattering depths: $\Lambda_{\text{eff}} = 4\,\text{nm}$ (blue circles), $\Lambda_{\text{eff}} = 18\,\text{nm}$ (red squares) and $\Lambda_{\text{eff}} = 180\,\text{nm}$ (green triangles), together with the best fit results (lines). Data points without error bars were fixed at an estimated value in the fit in order to decorrelate the parameters. The values at the lowest momentum transfer ($q = 2.8\,\text{nm}^{-1}$) are too high (see the discussion in the caption of figure 7), and are therefore excluded in the fit. Structural (c) and microscopic (d) relaxation times for $\Lambda_{\text{eff}} = 4\,\text{nm}$ (open circles) and $\Lambda_{\text{eff}} = 180\,\text{nm}$ (open triangles) together with the values derived from [10] for $\Lambda_{\text{eff}} = 4.6\,\text{nm}$ (full circles) and the bulk values (full triangles).

reduced scattering depths indicates a slowing down of the dynamics related to the collective rearrangement of the local structure at the surface. The slowing down is attributed to the loss of one degree of freedom for the molecular dynamics, which should, consequently, create a scenario similar to confined systems. The time scale of the microscopic relaxation is ten times faster than the structural one. Both structural and microscopic relaxation times tend to increase for smaller momentum transfer and, therefore, a linear fit was performed to determine their values at zero momentum transfer.

A further quantity that can be derived from the fit parameters is the momentum transfer-dependent longitudinal viscosity η_{L} (see equation (11)). The results for the different effective scattering depths are reported in figure 9. We find a trend to higher viscosities at the surface. The momentum transfer dependence of the longitudinal viscosity can empirically be described by an exponential decay [29, 38] $\eta_L(q) = \eta_{\text{L}} \text{e}^{-cq}$, where c is an empirical fitting constant. This is illustrated in figures 9(d)–(f). The increase in the longitudinal viscosity at $\Lambda_{\text{eff}} = 4\,\text{nm}$ by a factor of two is related to the increased relaxation times. Inspection of figures 9(b) and (c) reveals that these changes are mainly due to the structural component. The increased structural relaxation time in the near-surface region might originate from a slowing-down of the collective dynamics in the subsurface region due to a geometrical change in the packing fraction [40]. Arguing more intuitively, it could be induced by the reduced degrees of freedom for the particle motion due to layering. This result relates our experiment to other viscosity measurements on solid–liquid interfaces [41, 42], which also show such an increase.

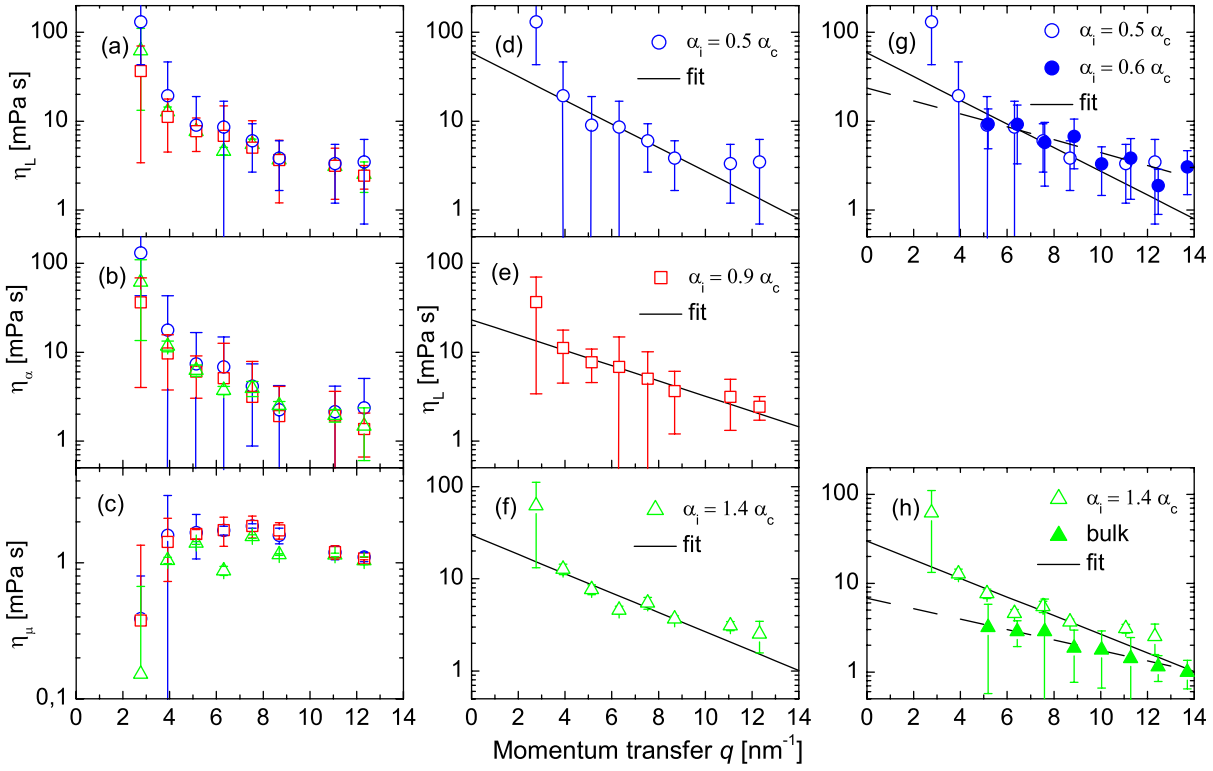

Figure 9. Longitudinal viscosity (a) together with its structural (b) and microscopic (c) components for different scattering depths: $\Lambda_{\mathrm{eff}} = 4\,\mathrm{nm}$ (blue circles), $\Lambda_{\mathrm{eff}} = 18\,\mathrm{nm}$ (red squares) and $\Lambda_{\mathrm{eff}} = 180\,\mathrm{nm}$ (green triangles). Panels (d)–(f) show the exponential momentum transfer dependence of the longitudinal viscosity together with the best-fit result. The values at the lowest momentum transfer ($q = 2.8\,\mathrm{nm}^{-1}$) are too high for the structural component and too low for the microscopic component (see the discussion in the caption of figure 7) and are therefore excluded from the fit. (g) Longitudinal viscosity for $\Lambda_{\mathrm{eff}} = 4\,\mathrm{nm}$ (open circles) together with the values derived from [10] for $\Lambda_{\mathrm{eff}} = 4.6\,\mathrm{nm}$ (full circle). (h) Longitudinal viscosity for $\Lambda_{\mathrm{eff}} = 180\,\mathrm{nm}$ (open triangles) together with the bulk values from [10] (full triangles).

Furthermore, it was observed that the layering of particles in glass-forming systems near a wall can be interpreted as a structural change due to confinement [43]. This interpretation is also well supported by recent simulations [44]. Indeed, the slowing down of the dynamics due to the layering of particles was shown in an experimental study of the glass transition of confined colloidal suspensions [45].

The values derived for the most surface-sensitive and bulk geometry are compared to the previous results [10] in figures 9(g) and (h). We note that the absolute values for the longitudinal viscosity coincide within the error bars for the surface-sensitive setup even though the capillary wave contribution was neglected in [10]. The values derived for $q = 0$ differ, however, significantly from our previous work. Due to the correlation of the fitted parameters, the error bars associated with the relaxation times and relaxation strengths are very large, even for spectra with very good statistics, thus leading to a large uncertainty in the derived viscosity

Table 1. Measured transport and dynamical properties of liquid indium at 170 °C for $q = 0$.

Λ_{eff} (nm)	v_{T} (m s^{-1})	v_{∞} (m s^{-1})	v_{a} (m s^{-1})	τ_{α} (ps)	τ_{μ} (ps)	η_{L} (mPa s)
4	1790 ± 12	2290 ± 35	2240 ± 15	1.4 ± 0.4	0.138 ± 0.008	60 ± 13
18	1790 ± 11	2290 ± 62	2240 ± 18	1.0 ± 0.2	0.123 ± 0.005	23 ± 7
180	1794 ± 4	2290 ± 16	2243 ± 7	0.8 ± 0.3	0.087 ± 0.001	30 ± 9

values. The bulk viscosities derived from the experiment in transmission geometry [10] lie systematically below the values for an effective scattering depth of $\Lambda_{\text{eff}} = 180$ nm.

Table 1 summarizes the obtained dynamical and transport properties for the measured scattering depths.

5. Conclusions and outlook

An investigation of the high-frequency dynamics of liquid indium in the near-surface region has been reported in this paper. The experiment was performed using IXS in grazing angle geometry. The recorded data were analysed within the framework of a generalized hydrodynamic theory. Extension of the memory function formalism by including a formalism for capillary waves facilitated a quantitative discrimination between density fluctuations in the isotropic bulk liquid and density fluctuations at the surface. The experimental data can be described with high accuracy by the given model function. The influence of capillary waves is visible in the spectra as an additional contribution with a Lorentzian shape in the investigated range of momentum and energy transfer. This effect is most pronounced for small momentum transfers and a probing depth of 4 nm. The contribution of capillary waves and bulk density fluctuations to the dynamical structure factor is in quantitative agreement with theory. The bulk density fluctuation contribution was shown to be influenced by the surface. A longer structural relaxation time at the surface was observed. The longitudinal viscosity increases by a factor of two in the near-surface region. The present study confirms the existence of this effect as observed previously and reinforces it with data of very high quality.

To address the universality of the observed phenomena, other systems need to be studied. Examples of good candidates include other liquid metals with a low melting point and a low vapour pressure. Gallium, mercury and lead are conceivable, but the preparation of a clean surface is more difficult. On the other hand, a surface-sensitive IXS study of liquids with a low electron density such as water or liquid alkanes is not feasible with the at present available photon flux due to the much weaker signal from low-Z materials and the shallower grazing angle of incidence required.

The dynamical structure factor was shown to feature contributions from density fluctuations and capillary waves. Since the contributions are coupled, it would be interesting to realize a liquid interface that suppresses capillary waves. This could be achieved by a liquid–solid interface that induces the same layering effect as the free surface. The search for a suitable confined system with a buried liquid interface without the capillary contributions is therefore of high interest. A recent publication [46] resolved the atomic-scale structure of a liquid metal–insulator interface. A similar stratification of the top most layers has been observed

with atomic resolution. The challenge for an IXS study of such an interface is the access of the liquid below the solid. The sapphire used as the confining solid is transparent for x-rays with an energy of 70 keV, but not for the energies used for IXS. The required energy resolution of a few meV is not achievable with high-energy x-rays. For an IXS study, one could imagine using a very thin film composed of a material with a low electron density as the confining solid.

Liquids are not the only disordered systems that show interesting surface effects. Several works point to the existence of an anomalous behaviour at the surface of glasses as well. In particular, a recent study [47] found changes in the boson peak at the surface with respect to the bulk. A depth-dependent study using IXS in grazing angle geometry would validate the intriguing helium scattering results and connect them with previous bulk measurements.

IXS is also an ideal tool for studying electron–phonon coupling and detecting Kohn anomalies [48] in charge density wave materials [49]. An interesting aspect is the surface-sensitive investigation of such anomalies. A first experiment [9] has successfully been performed showing indeed differences in the dispersion relation at the surface. A depth-resolved investigation of this effect and the study of similar systems could be an interesting extension of this work.

Finally, the grazing incidence setup could also be used for the investigation of lattice dynamics in thin films. The problem in studies of thin films composed of light materials is the strong decrease in the scattering signal due to the reduced scattering volume. Employing wave guide effects offers an elegant solution to this problem, since it enhances the signal by producing an x-ray standing wave between the substrate and the capping layer [50].

Acknowledgment

We thank the Max-Planck-Institut für Metallforschung (Stuttgart, Germany) for providing the sample environment, Denis Gambetti for his expert technical support and Jean Daillant for helpful discussions.

References

[1] Penfold J 2001 The structure of the surface of pure liquids *Rep. Prog. Phys.* **64** 777–814
[2] Parratt L G 1954 Surface studies of solids by total reflection of x-rays *Phys. Rev.* **95** 359–69
[3] Pershan P S 1994 The effects of surface profile and interface correlations on x-ray reflectivity from fluid interfaces *J. Phys.: Condens. Matter* A **6** 37
[4] Magnussen O M, Ocko B M, Regan M J, Penanen K, Pershan P S and Deutsch M 1995 X-ray reflectivity measurements of surface layering in liquid mercury *Phys. Rev. Lett.* **74** 4444–7
[5] Kress W and de Wette F W 1991 *Surface Phonons* (*Series in Surface Science* vol 21) (Berlin: Springer)
[6] Hulpke E 1992 *Helium Atom Scattering from Surfaces* (*Series in Surface Science* vol 27) (Berlin: Springer)
[7] Ruocco G, Sette F, Bergmann U, Krisch M, Masciovecchio C, Mazzacurati V, Signorelli G and Verbeni R 1996 Equivalence of the sound velocity in water and ice at mesoscopic wavelengths *Nature* **379** 521–3
[8] Dosch H, Batterman B W and Wack D C 1986 Depth-controlled grazing-incidence diffraction of synchrotron x-radiation *Phys. Rev. Lett.* **56** 1144–7
[9] Murphy B M, Requardt H, Stettner J, Serrano J, Krisch M, Müller M and Press W 2005 Phonon modes at the 2H-$NbSe_2$ surface observed by grazing incidence inelastic x-ray scattering *Phys. Rev. Lett.* **95** 256104
[10] Reichert H, Bencivenga F, Wehinger B, Krisch M, Sette F and Dosch H 2007 High-frequency subsurface and bulk dynamics of liquid indium *Phys. Rev. Lett.* **98** 096104

[11] Tostmann H, DiMasi E, Pershan P S, Ocko B M, Shpyrko O G and Deutsch M 1999 Surface structure of liquid metals and the effect of capillary waves: x-ray studies on liquid indium *Phys. Rev.* B **59** 783–91
[12] Boon J P and Yip S 1980 *Molecular Hydrodynamics* (New York: Dover)
[13] Pecora R 1985 *Dynamic Light Scattering Applications of Photon Correlation Spectroscopy* (New York: Plenum)
[14] Lovesey S W and Springer T 1977 *Dynamics of Solids and Liquids by Neutron Scattering* (Berlin: Springer)
[15] Schülke W 2005 *Electron Dynamics by Inelastic X-Ray Scattering* (Oxford: Oxford University Press)
[16] Mora S and Daillant J 2002 Height and density correlations at liquid surfaces: application to x-ray scattering *Eur. Phys. J.* B **27** 417–28
[17] Loudon R 1980 Theory of thermally induced surface fluctuations on simple fluids *Proc. R. Soc.* A **372** 275–95
[18] Forster D 1975 *Hydrodynamic Fluctuations, Broken Symmetry, and Correlation Functions* (Reading, MA: Addison-Wesley)
[19] Kadanoff L P and Martin P C 1963 Hydrodynamic equations and correlation functions *Ann. Phys.* **24** 419
[20] Loudon R 1984 Ripples on liquid interfaces, surface excitations *Modern Problems in Condensed Matter Science* **9** 589–638
[21] Iida T and Guthrie R 1988 *The Physical Properties of Liquid Metals* (Oxford: Clarendon)
[22] *Handbook of Chemistry and Physics* http://www.hbcpnetbase.com/
[23] White D W G 1972 The surface tensions of indium and cadmium *Metall. Mater. Trans.* B **3** 1933–6
[24] Beer S Z 1988 *Liquid Metals* (New York: Marcel Dekker)
[25] Kamioka H 1983 Change of ultrasonic wave velocity in indium near the melting point *J. Phys. Soc. Japan* **52** 2784–9
[26] Duggin M J 1972 The thermal conductivities of liquid lead and indium *J. Phys. F: Met. Phys.* **2** 433
[27] Mori H 1965 Transport, collective motion and Brownian motion *Prog. Theor. Phys.* **33** 423
[28] Balucani U and Zoppi M U 1994 *Dynamics of the Liquid State* (Oxford: Carendon)
[29] Scopigno T, Ruocco G and Sette F 2005 Microscopic dynamics in liquid metals: the experimental point of view *Rev. Mod. Phys.* **77** 881–933
[30] Monaco G, Cunsolo A, Ruocco G and Sette F 1999 Viscoelastic behavior of water in the terahertz-frequency range: an inelastic x-ray scattering study *Phys. Rev.* E **60** 5505–21
[31] Litovitz T A and Davis C M 1965 *Physical Acoustics* (New York: Academic)
[32] Götze W and Lücke M 1975 Dynamical current correlation functions of simple classical liquids for intermediate wave numbers *Phys. Rev.* A **11** 2173–90
[33] Dosch H 1992 *Critical Phenomena at Surfaces and Interfaces. Evanescent X-Ray and Neutron Scattering* (*Springer Tracts in Modern Physics*) (Berlin: Springer)
[34] Ruocco G and Sette F 2003 Inelastic x-ray scattering: a new spectroscopy tool to investigate the atomic dynamics in condensed matter *Synchrotron Radiation: Fundamentals, Methodologies and Applications Conf. Proc.* **82** ed S Mobilio and G Vlaic (Bologna, Società Italiana di Fisica)
[35] Burkel E 2000 Phonon spectroscopy by inelastic x-ray scattering *Rep. Prog. Phys.* **63** 171–232
[36] Roth A 1982 *Vacuum Technology* (Amsterdam: North-Holland)
[37] *Cern program library long writeup d506* online http://wwwasdoc.web.cern.ch/wwwasdoc/minuit/minmain.html
[38] Bencivenga F, Cunsolo A, Krisch M, Monaco G, Ruocco G and Sette F 2009 High frequency dynamics in liquids and supercritical fluids: a comparative inelastic x-ray scattering study *J. Chem. Phys.* **11** 064501
[39] Kleppa O J 1950 Ultrasonic velocities of sound in some metallic liquids. adiabatic and isothermal compressibilities of liquid metals at their melting points *J. Chem. Phys.* **18** 1331
[40] Watanabe K and Tanaka H 2008 Direct observation of medium-range crystalline order in granular liquids near the glass transition *Phys. Rev. Lett.* **100** 158002
[41] Patyonin S I and Regel A R 1964 On the manifestation of structural viscosity in the surface layers of liquid metals *Ukr. Fiz. Zh.* **9** 471
[42] Raviv U, Laurat P and Klein J 2001 Fluidity of water confined to subnanometre films *Nature* **413** 51

[43] Fehr T and Löwen H 1995 Glass transition in confined geometry *Phys. Rev.* E **52** 4016–25
[44] Mittal J, Truskett T M, Errington J R and Hummer G 2008 Layering and position-dependent diffusive dynamics of confined fluids *Phys. Rev. Lett.* **100** 145901
[45] Nugent C R, Edmond K V, Patel H N and Weeks E R 2007 Colloidal glass transition observed in confinement *Phys. Rev. Lett.* **99** 025702
[46] Tamam L, Pontoni D, Hofmann T, Ocko B M, Reichert H and Deutsch M 2010 Atomic-scale structure of a liquid metal-insulator interface *J. Phys. Chem. Lett.* **1** 1041–5
[47] Steurer W, Apfolter A, Koch M, Ernst W E, Søndergård E, Manson J R and Holst B 2008 Anomalous phonon behavior: blueshift of the surface boson peak in silica glass with increasing temperature *Phys. Rev. Lett.* **100** 135504
[48] Baron A Q R, Uchiyama H, Tanaka Y, Tsutsui S, Ishikawa D, Lee S, Heid R, Bohnen K-P, Tajima S and Ishikawa T 2004 Kohn anomaly in MgB_2 by inelastic x-ray scattering *Phys. Rev. Lett.* **92** 197004
[49] Wilson J A, Di F J and Salvo Mahajan S 1974 Charge-density waves in metallic, layered, transition-metal dichalcogenides *Phys. Rev. Lett.* **32** 882
[50] Wang J J, Bedzyk M J and Caffrey M 1992 Resonance-enhanced x-rays in thin films: a structure probe for membranes and surface layers *Science* **258** 775–8